Journal of Magnetics 9(2), 52-59 (2004)

Interlayer and Interfacial Exchange Coupling of IrMn Based MTJ

J. Wrona[1]*, T. Stobiecki[1], M. Czapkiewicz[1], J. Kanak[1], R. Rak[1], M. Tsunoda[2] and M. Takahashi[2]

[1]*Department of Electronics, University of Science and Technology, 30-059 Krakow, Poland*
[2]*Tohoku University, Department of Electronic Engineering, Sendai 980-8579, Japan*

(Received 4 June 2004)

As deposited and annealed MTJs with the structure of Ta(5 nm)/Cu(10 nm)/Ta(5 nm)/$Ni_{80}Fe_{20}$(2 nm)/Cu(5 nm)/$Ir_{25}Mn_{75}$(10 nm)/$Co_{70}Fe_{30}$(2.5 nm)/Al-O/$Co_{70}Fe_{30}$(2.5 nm)/$Ni_{80}Fe_{20}$(t)/Ta(5 nm), where t = 10, 30, 60 and 100 nm were characterized by XRD and magnetic hysteresis loops measurements. The XRD measurements were done in grazing incidence (GID scan-2θ) and θ-2θ geometry, by rocking curve (scan-ω) and pole figures in order to establish correlation between texture and crystallites size and magnetic parameters of exchange biased and interlayer coupling. The variations of shifting and coercivity field of free and pinned layers after annealing in 300°C correlate with the improvement of [111] texture and grains size of $Ni_{80}Fe_{20}$ and $Ir_{25}Mn_{75}$ respectively. The exchange biased and the coercivity fields of the pinned layer linearly increased with increasing grain size of $Ir_{25}Mn_{75}$. The reciprocal proportionality between interlayer coupling and coercivity fields of the free layer and grain size of $Ni_{80}Fe_{20}$ was found. The enhancement of interlayer coupling between pinned and free layers, after annealing treatment, indicates on the correlated in-phase roughness of dipolar interacting interfaces due to increase of crystallites size of $Ni_{80}Fe_{20}$.

Key words : *interlayer and interfacial exchange coupling, XRD, MOKE and R-VSM magnetometers*

1. Introduction

For read head and M-RAM arrays applications, spin valve or magnetic tunnel junction (MTJ) films with: large exchange biased field (H_{EB}), high magnetoresistance (MR) or tunnel magnetoresistance (TMR), high blocking temperature, low interlayer coupling, and coercivity fields are required. Compared to other antiferromagnets (AF) like FeMn, NiO, CrMnPt, and PtMn [1], $Ir_{25}Mn_{75}$ has been found as the very promising AF material due to its high exchange bias energy ($J_{EB} \approx 4 \times 10^{-4}$ J/m^2), high blocking temperature ($T_b \approx 590$ K) and low critical thickness (~7 nm) [2]. The exchange coupling between (AF)/ferromagnetic (F) layers, which has been shown primarily to be an interfacial phenomenon [3], should be dependent on the microstructural characteristics of the films such as crystal texture, grain size and roughness. All these factors influence on the interface microstructure and are closely linked to the structure of the growth/buffer and underlayers which are used in designed junctions [4, 5]. The large exchange bias field values reported in the literature [5-8] are associated with an increase of the (111)-fcc texture and grain size obtained after annealing [9, 10], but also some contrary opinions have been given in the literature either [11].

In this work we discuss diffraction measurements for as deposited and annealed junctions with the structure of Ta(5 nm)/Cu(10 nm)/Ta(5 nm)/$Ni_{80}Fe_{20}$(2 nm)/Cu(5 nm)/$Ir_{25}Mn_{75}$(10 nm)/$Co_{70}Fe_{30}$(2.5 nm)/Al-O/$Co_{70}Fe_{30}$(2.5 nm)/$Ni_{80}Fe_{20}$(t)/Ta(5 nm), where t = 10, 30, 60 and 100 nm, in order to establish correlation between structure ((111)-fcc texture and grain size of Cu, $Ir_{25}Mn_{75}$ and $Ni_{80}Fe_{20}$ sublayers of the stack) and magnetic parameters of interfacial and interlayer exchange coupling. Bearing in mind potential applications point of view, the thickness of free layer of MTJ should be as thin as possible, however XRD measurements are sufficiently accurate for thicknesses greater than 10 nm.

2. Structure of Measured Sample

The tunnel junctions with the structure given in Fig. 1a, were prepared in Prof. M. Takahashi laboratory at Tohoku University, on thermally oxidized Si wafers using DC magnetron sputtering with ultra clean Ar(9 N) as the

*Corresponding author: Tel: (+4812) 6173044, e-mail: wrona@agh.edu.pl

process gas, in a chamber with base pressure of 4×10^9 hPa. On the buffer layers system Ta(5 nm)/Cu(10 nm)/ Ta(5 nm)/$Ni_{80}Fe_{20}$(2 nm)/Cu(5 nm), which was deposited to induce (111) - fcc plane texture and transfer it to the next overlayers, the antiferromagnetic layer of $Ir_{25}Mn_{75}$ of the thickness of 10 nm was deposited in order to shift the hysteresis loop of pinned layer ($Co_{70}Fe_{30}$-2.5 nm) from the zero field by exchange biasing. The barrier formation was performed by deposition of the 1.5 nm thick metallic Al film and subsequently oxidizing it in the oxidization chamber having a radial line slot antenna (RLSA) for 2.45 GHz-microwave. The details of this plasma oxidization technique are explained elsewhere [12]. The free layer is composed of 2.5 nm layer of $Co_{70}Fe_{30}$ and another one of $Ni_{80}Fe_{20}$ of variable thickness from 10 nm to 100 nm. To prevent oxidation the whole sample was capped by 5 nm Ta. The small magnetic field of 2.4 kA/m was applied parallel to the films plane during deposition of the ferromagnetic ($Co_{70}Fe_{30}$ and $Ni_{80}Fe_{20}$) and $Ir_{25}Mn_{75}$ layers. The samples were annealed in vacuum (10^{-6} hPa) in a magnetic field of 80 kA/m, followed by field cooling. These are optimum annealing conditions to obtain maximum of tunnelling MR ratio [13]. For structure and magnetic measurements the sample in diameter of 10 mm was prepared (Fig. 1b).

3. Measurement Tools

The magnetic measurements were performed by R-VSM (Resonance Vibrating Sample Magnetometers) and MOKE (Magnetooptical Kerr Effect) magnetometers. R-VSM measurement delivers information about averaged magnetization process from the whole volume of the sample, whereas magnetooptical information from MOKE magnetometer is local, limited by light-beam spot and depth

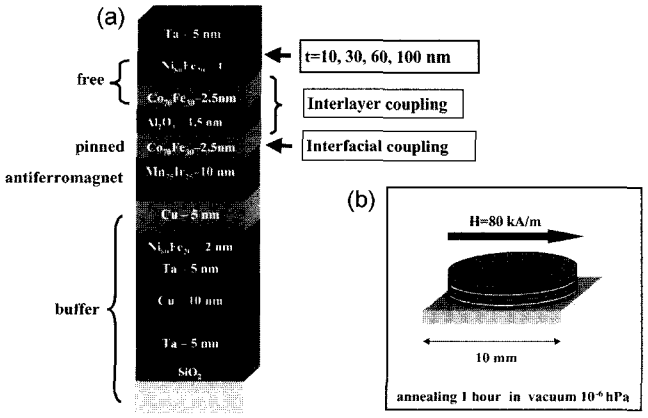

Fig. 1. (a) Multilayer structure of MTJ; (b) annealing conditions of investigated samples.

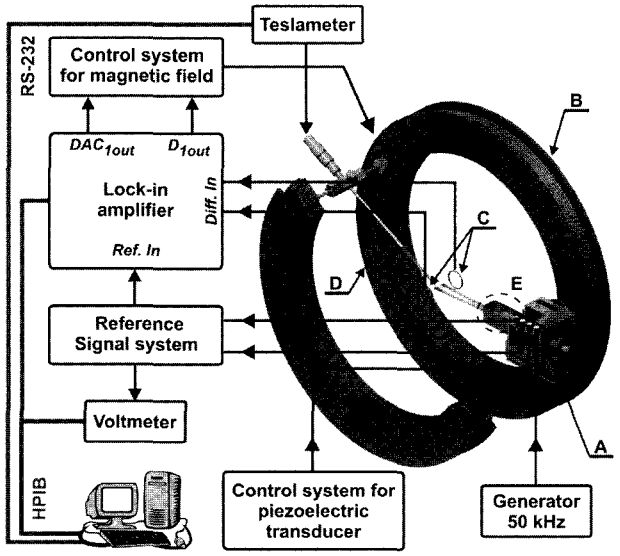

Fig. 2. Block diagram of R-VSM; A - head, B - Helmholtz coils, C - pick-up coils, D - Hall probe, E - capacity sensor of the sample position.

with an exponential decay. Block diagram of R-VSM is shown in Fig. 2. There are the following main advantages of R-VSM in relation to the classical Foner's VSM [14]: sample oscillates in parallel to the direction of external magnetic field, therefore it is always in the region of homogeneous field (in the Foner's VSM sample vibrates perpendicularly to the direction of external magnetic field), the configuration of pick-up coils in the form of small Smith coils is more favourable [15] than two pairs of pick-up coils connected adversely as in conventional Foner's VSM, and the oscillations of the sample are more stable due to controlled resonance frequency by amplifier with negative feedback. The detailed description of R-VSM was described in [16-18]. Due to high sensitivity

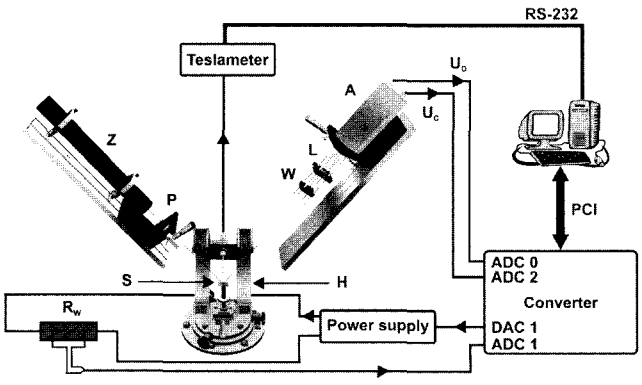

Fig. 3. Schematic layout of MOKE system; Z - laser, P - polarizer, W - Wollaston prism, L - lens, A - differential amplifier, H - Helmholtz coils.

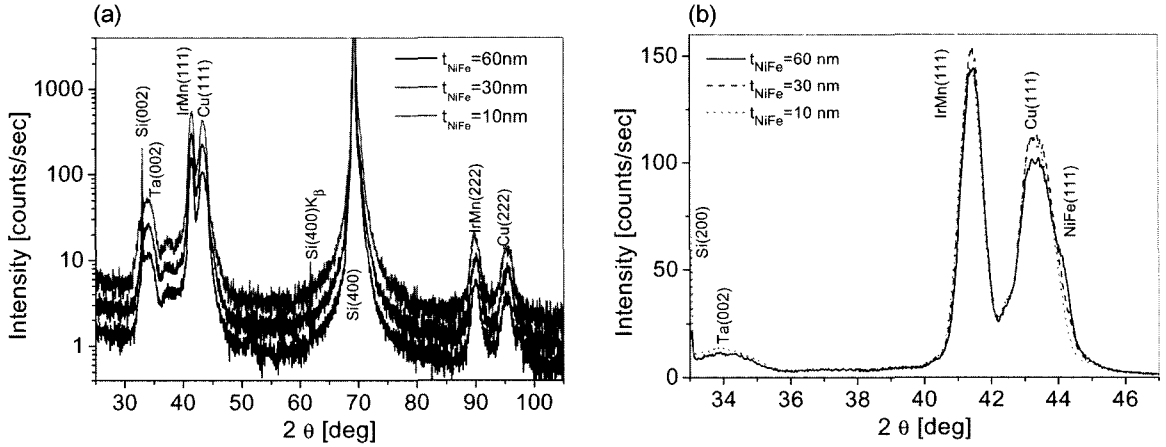

Fig. 4. XRD θ-2θ profiles for as-deposited MTJ (t = 10, 30, 60 nm), (a) wide range of diffraction angle 2θ where first and second order peaks of Cu and $Ir_{25}Mn_{75}$ are observed (b) narrow range of 2θ.

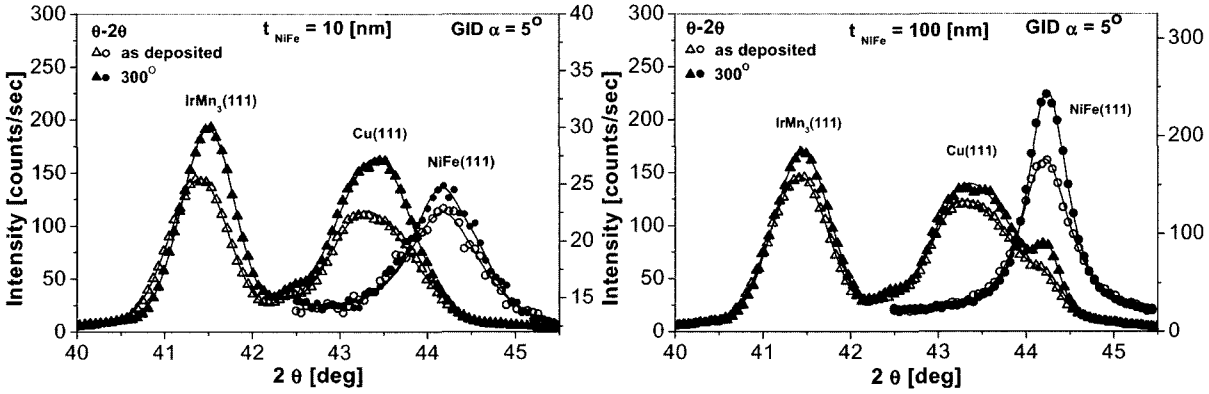

Fig. 5. θ-2θ and 2θ-GID scans for as-deposited and annealed MTJ (t = 10 and 100 nm) with fitting lines of fcc-(111)$Ir_{25}Mn_{75}$, (111)Cu and (111)$Ni_{80}Fe_{20}$ peaks.

(better than 10^{-5} emu), R-VSM can measure major and minor hysteresis loops of MTJ very precisely.

The arrangement for measurements of MOKE hysteresis loop is shown in Fig. 3. The system is especially recommended for rapid measurements up to 1500 field steps per second. Using Wollaston prism and low noise differential amplifier [17-19], very high angle resolution of Kerr rotation (10^{-3} min) was obtained.

In order to find the correlation between structure parameters and magnetic properties, the samples have been characterized by XRD experiment, using Philips diffractometer type XPert MPD with Cu-anode in θ-2θ geometry, Grazing Incidence Diffracion method - GID (scan-2θ), by rocking curve (scan-ω) and pole figure scan.

4. Results and Discussion

4.1. Structure measurements

Figure 4a shows specular XRD-profiles measured in wide range of diffraction angle 2θ for a series of as deposited MTJs with different free layer thicknesses. Except of Si - substrate peaks, only β-Ta (002) and strong fcc textured peaks of $Ir_{25}Mn_{75}$ and Cu are observed (Fig. 4b). Figure 5 shows the scans of θ-2θ and GID for the as-deposited and annealed samples where fcc peaks of (111)$Ir_{25}Mn_{75}$, (111)Cu and (111)$Ni_{80}Fe_{20}$ are observed. Due to very close lattice planes of (111)Cu and (111)-$Ni_{80}Fe_{20}$ GID measurement (under $\alpha = 5°$) allowed for the separation of Cu and $Ni_{80}Fe_{20}$ peaks. The annealing treatment in vacuum at 300 °C for 1 hour, induces an increase in (111) peaks intensity and a slight peak shift to higher 2θ position indicates an improvement in crystallinity [6] of the multilayer structure.

The crystallite size of (111)$Ir_{25}Mn_{75}$, (111)Cu from θ-2θ-scans, and (111)$Ni_{80}Fe_{20}$ from GID-scans were determined, using high purity powder standard for calibration and program *Line Profile Analysis (LPA)*. Figure 6 shows examplary scans of θ-2θ and GID for as deposited and

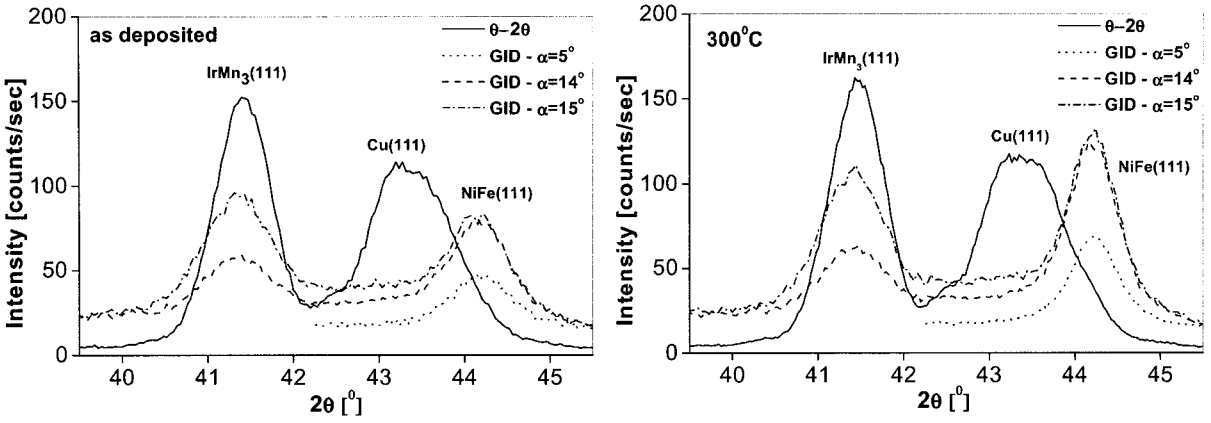

Fig. 6. θ-2θ and GID scans for as deposited (a) and annealed sample (b) with t_{NiFe} = 30 nm.

annealed sample with t_{NiFe} = 30 nm. GID scans (under α = 5°) show only reflections from (111) $Ni_{80}Fe_{20}$ planes, none Cu and $Ir_{25}Mn_{75}$ peaks are observed, but only the increase of the incidence beam angle up to 14° show reflections from (111)$Ir_{25}Mn_{75}$ planes. It means that lattice planes of Cu are very well parallel to the substrate plane in contrary to the lattice planes of $Ir_{25}Mn_{75}$ and $Ni_{80}Fe_{20}$. Typical rocking curves of $Ir_{25}Mn_{75}$(111) and Cu(111), for as deposited and annealed sample with t = 10 nm, are shown, in Fig. 7a and Fig. 7b, respectively. The rocking curve peaks are symmetrical and centred at Bragg positions of $Ir_{25}Mn_{75}$(111) and Cu(111). The annealing treatment in vacuum at 300 °C for 1 hour, induces an increase in (111) peak intensity and crystallite size which leads in consequence to the linear decrease of FWHM vs. increasing of $Ir_{25}Mn_{75}$ and Cu grain size. The lattice

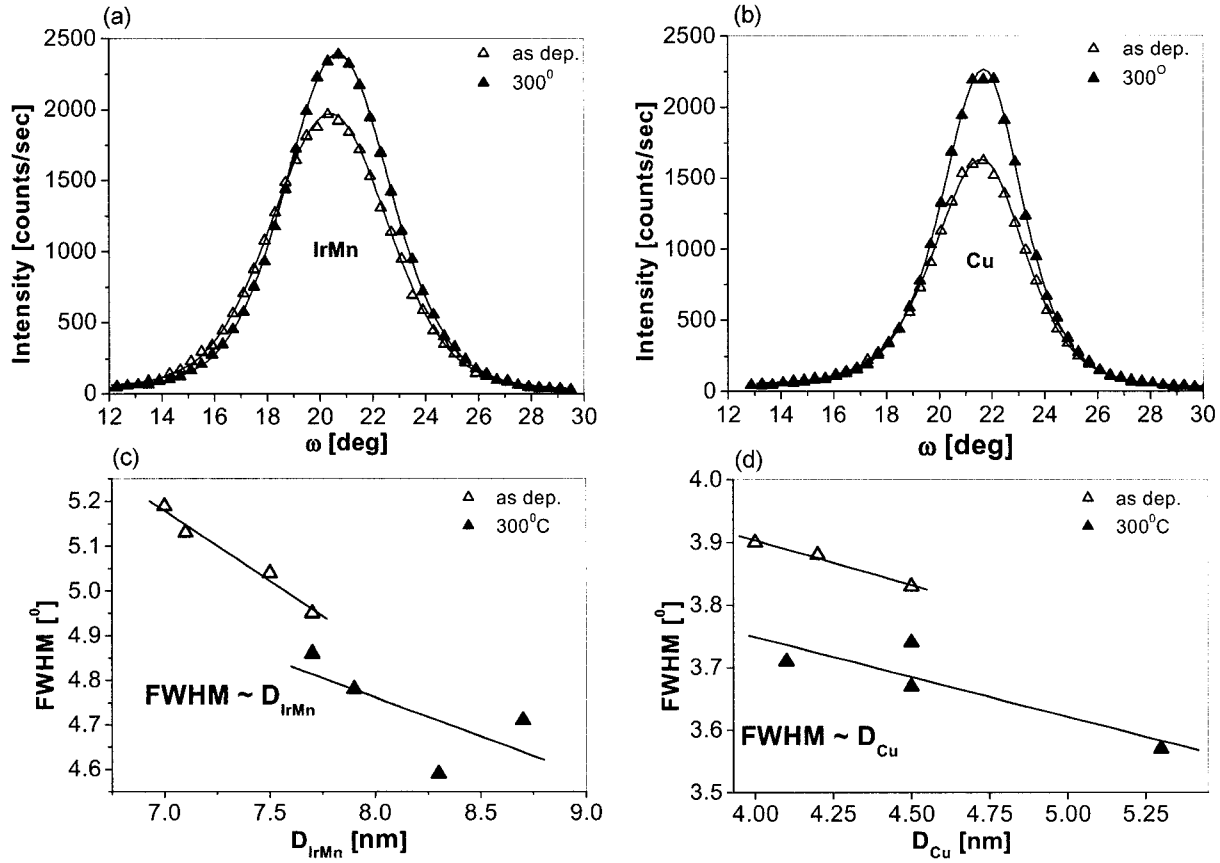

Fig. 7. Example of rocking curves w-scans for as-deposited and annealed MTJ (t = 10 nm) with fitting lines of fcc-(111)$Ir_{25}Mn_{75}$ (a) and (111)Cu (b). FWHM vs. grain size of $Ir_{25}Mn_{75}$ (c) and Cu (d) for as-deposited and annealed samples.

Table 1. Structure parameters of $Ir_{25}Mn_{75}$ and Cu where t, a, D are given in nm and FWHM in angle degrees.

MTJ	$Ir_{25}Mn_{75}$						Cu					
	as-deposited			annealed 300 °C			as-deposited			annealed 300 °C		
t	a	D	FWHM	a	D	FWHM	A	D	FWHM	a	D	FWHM
10	0.3776	7.0	5.19	0.3767	8.7	4.71	0.3618	4.7	4.07	0.3608	5.3	3.57
30	0.3772	7.5	5.04	0.3769	7.9	4.78	0.3614	4.2	3.88	0.3613	4.5	3.74
60	0.3771	7.7	4.95	0.3768	8.3	4.59	0.3616	4.0	3.90	0.3615	4.1	3.71
100	0.3774	7.1	5.13	0.3771	7.7	4.86	0.3619	4.5	3.83	0.3614	4.5	3.67

Table 2. Structure and magnetic parameters of $Ni_{80}Fe_{20}$, where H_S and H_{CF} are given in A/m.

MTJ	$Ni_{80}Fe_{20}$							
	as-deposited				annealed 300 °C			
t	a	D	H_S	H_{CF}	a	D	H_S	H_{CF}
10	0.3553	7.8	760	943	0.3553	10.1	935	764
30	0.3552	10.5	168	527	0.3548	14.3	465	282
60	0.3549	11.4	139	397	0.3547	31.7	192	177
100	0.3548	14.3	60	306	0.3545	41.7	149	243

constants and FWHM of the $Ir_{25}Mn_{75}(111)$, and Cu(111)-rocking curve peaks decrease (Table 1), indicating an improvement in texture of multilayer structure. The lattice constants and grain sizes of $Ni_{80}Fe_{20}$ determined from GID measurements, are collected in Table 2. The typical pole figures of $Ir_{25}Mn_{75}$ and Cu for as-deposited and annealed samples (Fig. 8) represent centred [111] spots and spread rings around the angle y = 70°. Narrower and

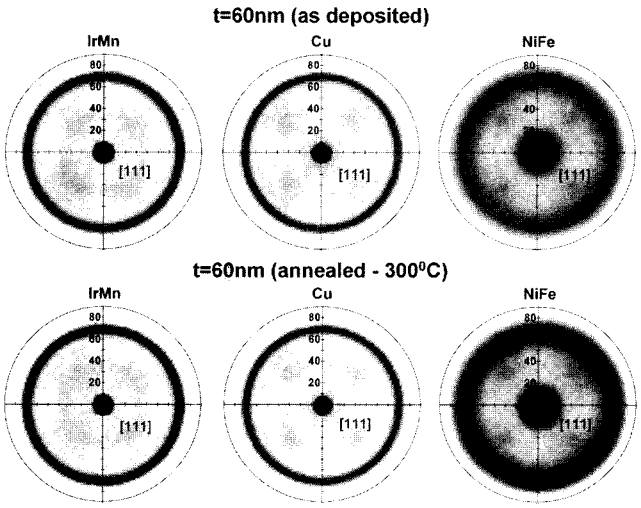

Fig. 8. Exemplary pole figures of MTJ (t = 60 nm) for as-deposited: $Ir_{25}Mn_{75}\{111\}$, Cu{111}, $Ni_{80}Fe_{20}\{111\}$ and annealed: $Ir_{25}Mn_{75}\{111\}$, Cu{111}, $Ni_{80}Fe_{20}\{111\}$.

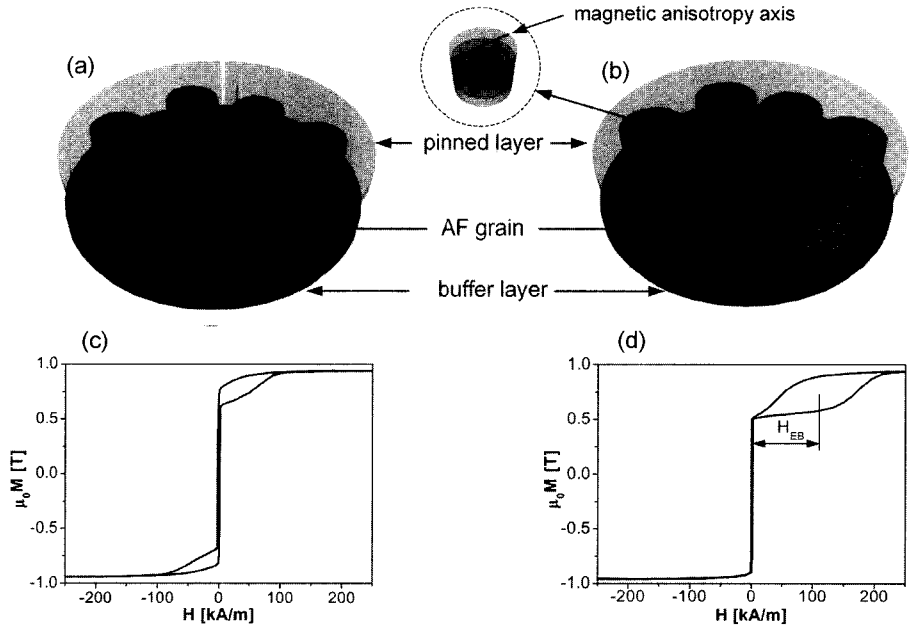

Fig. 9. Schematic view of a single spin ensemble (SSEM) for as deposited (a) and annealed (b) samples. Corresponding hysteresis loops: as deposited (c), annealed (d) are below.

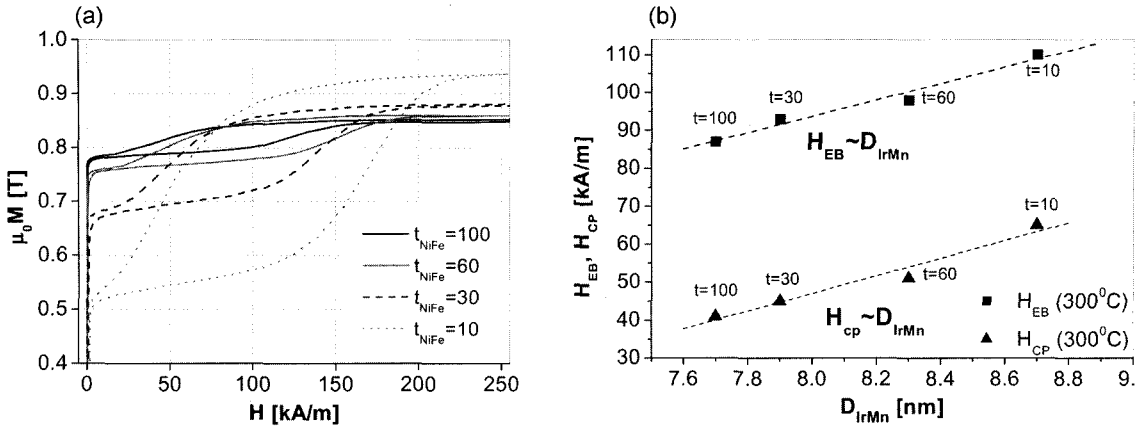

Fig. 10. (a) Exchange biased (H_{EB}) and coercivity fields (H_{CP}) as a function of grain size of $Ir_{25}Mn_{75}$ (D_{IrMn}), (b) the hysteresis loops of pinned layer with t_{CoFe} = 2.5 nm for series of annealed samples.

higher intensity rings are observed for annealed samples. The (111) planes of $Ir_{25}Mn_{75}$ and Cu are parallel to the substrate surface, which means that the sample has a (111) sheet texture with no crystallographic orientation in the film plane. The pole figure of $Ni_{80}Fe_{20}$ (accurately measured only for $Ni_{80}Fe_{20}$ layers thicker than 30 nm) represent wide spot [111] and weak diffuse ring in as deposited samples which means that $Ni_{80}Fe_{20}$ crystallites are disoriented from [111] direction. After annealing the intensity of the central spot and ring around the angle ψ =

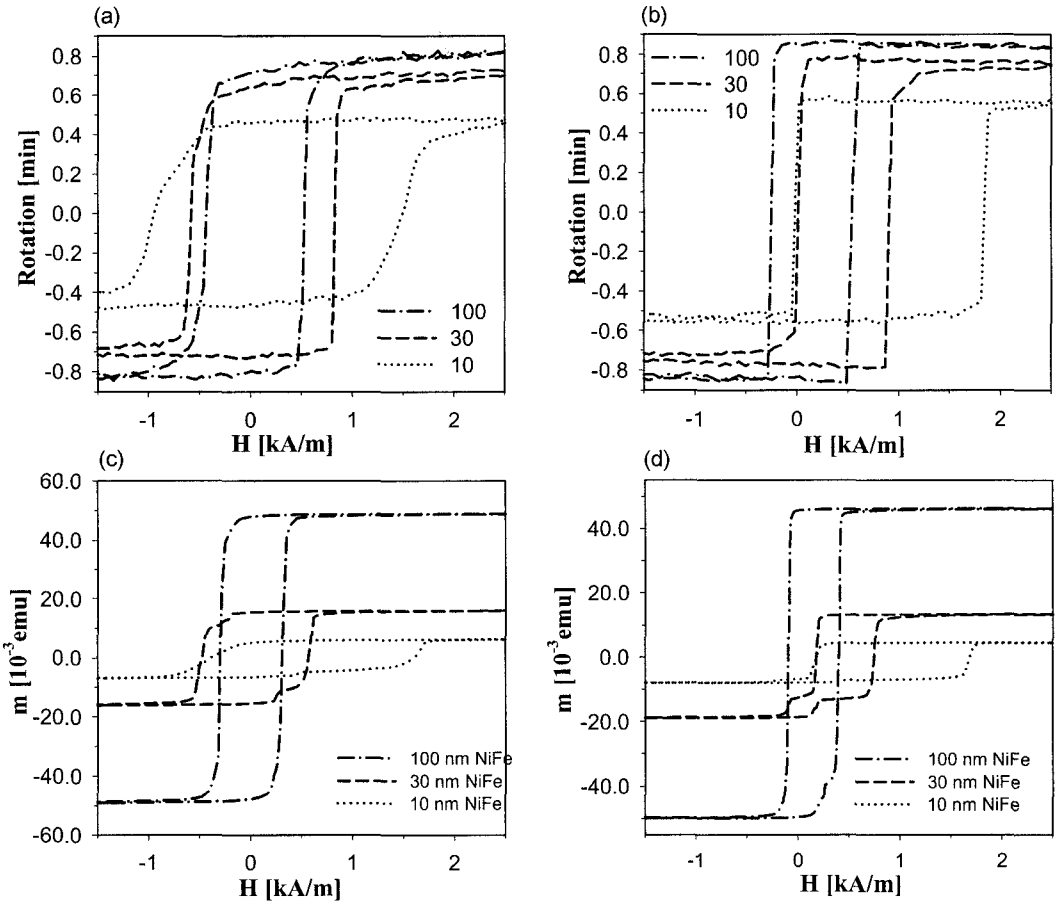

Fig. 11. The minor hysteresis loops measured by MOKE (a, b) and R-VSM magnetometers (c, d) for as deposited (a, c) and annealed (b, d) samples. Note the small hysteresis loop from $Ni_{80}Fe_{20}$ (2 nm) buffer layer, detected only by R-VSM measurements.

70° increases while FWHM decreases. These changes lead to the improvement of the (111) plane texture of $Ni_{80}Fe_{20}$.

4.2. Interfacial exchange coupling

Figure 9 shows a schematic view of the single spin ensemble model (SSEM) proposed by Tsunoda [20]. The ferromagnetic pinned layer (FP) is regarded as a single domain and antiferromagnetic (AF) layer as an aggregation of the AF grains whose magnetocrystalline anisotropy has uniaxial symmetry. The anisotropy axes of the AF grains are randomly distributed in the film plane. Here it was assumed that the intergranular magnetic coupling of the AF grains was neglected and that the single spin coupling is applicable between the FP layer and each AF grains. The hysteresis loop for as deposited sample is not biased (Fig. 9c) due to magnetically disordered AF grains (Fig. 9a). The thermal annealing, close to the blocking temperature and followed by magnetic field cooling, results in magnetizations ordering of AF grains in direction of external magnetic field where the x-components of AF magnetization are positive (Fig. 9b). In this case the hysteresis loop of the FP layer is biased, as shown in Fig. 9d. The exchange biased fields of pinned layer with constant thickness ($t_{CoFe} = 2.5$ nm) are different in particular samples, as shown in Fig. 10a, due to the changes of AF ($Ir_{25}Mn_{75}$) grains size. The mutual correlations between grain size, exchange biased and coercivity field of annealed junctions are illustrated in Fig. 10b. Accompanied by the change of grain size of $Ir_{25}Mn_{75}$, the linear increase in exchange biased H_{EB} and coercivity H_{CP} fields of pinned layer $Co_{70}Fe_{30}$ was observed (Fig. 5). Maximum value of $H_{EB} = 110$ kA/m (which corresponds to $J_{EB} = 3.6 \times 10^{-4}$ J/m^2) is reached for sample of t = 10 nm whose grain size increases by 24% going from as deposited state to annealed one.

4.3. Interlayer exchange coupling

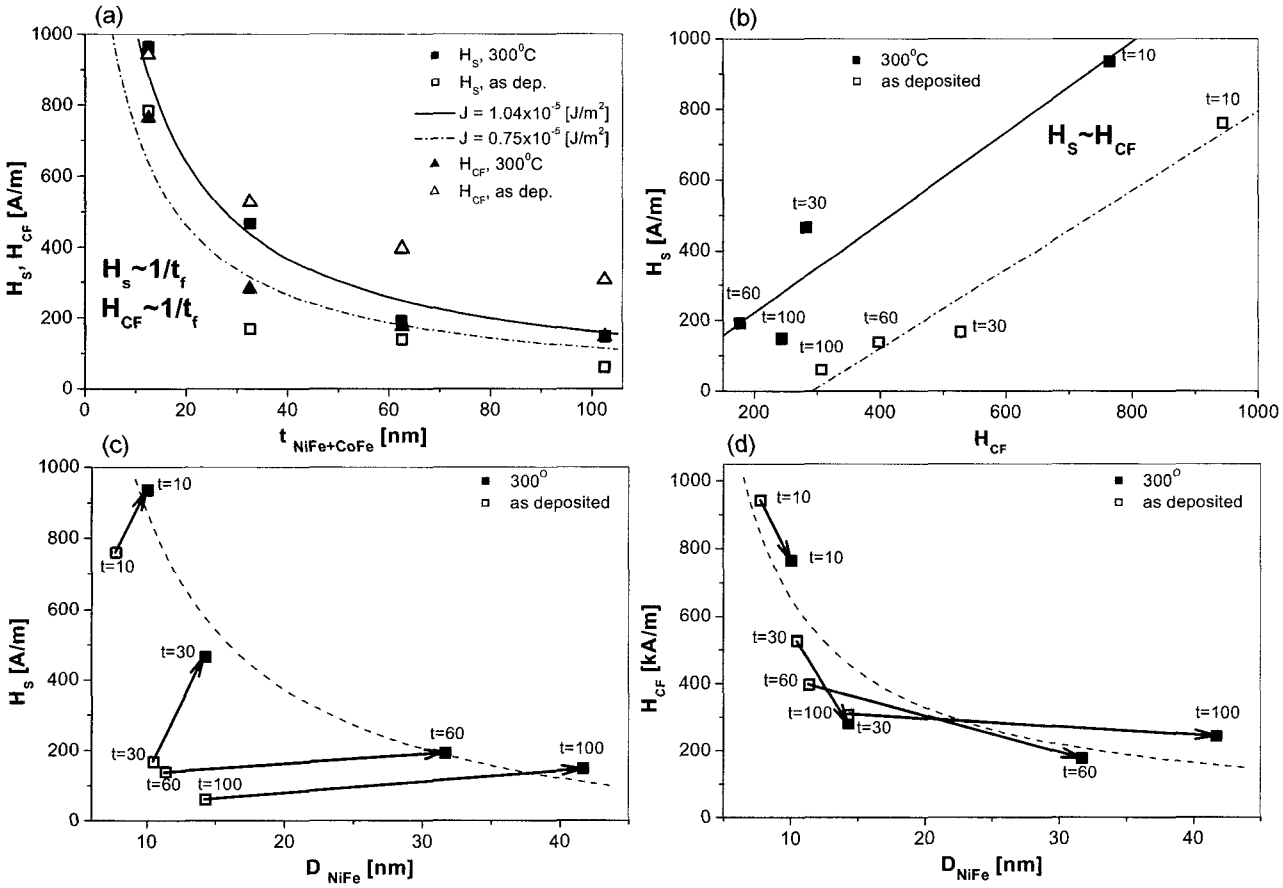

Fig. 12. (a) The interlayer coupling field and coercivity field for as deposited and annealed junctions vs. free layer thickness. (b) The linear correlation between interlayer coupling field and coercivity field of the free layer. (c) The interlayer coupling field vs. grain size of $Ni_{80}Fe_{20}$. (d) The coercivity field of the free layer vs. grain size of $Ni_{80}Fe_{20}$. The solid and dotted lines in (a) an (b) are fits. The dashed lines in (c) and (d) are guides to the eyes, representing reciprocal proportionality. Arrows in (c) and (d) between empty (as deposited) and solid (annealed) points illustrate the changes in the grain size of $Ni_{80}Fe_{20}$ after annealing of MTJs.

Fig. 11 shows the magnetization minor hysteresis loops measured by MOKE (Fig. 11a, b) and R-VSM (Fig. 11c, d) magnetometers. As deposited samples are characterized by oblique hysteresis loops, large coercivity and slow switching (Fig. 11a, c) while the annealed ones - by rectangular hysteresis, fast switching and smaller coercivity (Fig. 11b, d). The minor loops are always shifted in the direction indicating a ferromagnetic coupling between pinned ($Co_{70}Fe_{30}$) and free ($Co_{70}Fe_{30} + Ni_{80}Fe_{20}$) layers which originates from the dipolar magnetic coupling (known as Nèel coupling or "orange peel" coupling). The decrease of interlayer coupling ($H_S = J/m_0M_Ft_F$) and coercivity (H_{CF}) fields of the free layer with increasing $Ni_{80}Fe_{20}$ thickness (Fig. 12a and Table 2) in as-deposited and annealed samples, were observed. After annealing the interlayer coupling energy increases from $J = 0.75 \times 10^{-5}$ J/m^2 to 1.04×10^{-5} J/m^2 whereas H_{CF} of free layer decreases. The variations of H_S and H_{CF} for as deposited and annealed junctions are correlated linearly (Fig. 12b). The enhancement of interlayer coupling between pinned and free layers after thermal annealing indicates the correlated in-phase roughness of dipolar interacting interfaces - according to the model of columnar structure with conformal waviness proposed by Kools *et al.* [21] - due to the increase of crystallites size of $Ni_{80}Fe_{20}$. From the plots for the changes of H_S and H_{CF} as a function of the crystallite size of $Ni_{80}Fe_{20}$ (D_{NiFe}), we found that H_{CF} follows the $1/D_{NiFe}$ dependence (compare the empty and solid squares for the particular $Ni_{80}Fe_{20}$ thickness in Fig. 12d), but H_S for as deposited samples does not follow it (Fig. 12c). This contrast is owing to the remarkably small H_S against H_{CF} in as-deposited films as shown in Fig. 12b and indicates the difference of the lateral correlation length of the respective interlayer-coupling phenomenon. Taking into account that the pinned layer magnetization of as-deposited films makes domain structure in the film plane under the small field range, in which the free layer switches its magnetization (as shown in Fig. 9a), we can conclude that the lateral correlation length of H_S is longer than that of H_{CF}.

5. Conclusions

Complete and systematic XRD measurements indicate improvement of (111)-fcc texture of Cu, $Ir_{25}Mn_{75}$ and $Ni_{80}Fe_{20}$ planes, and the enlarged crystallites size of $Ir_{25}Mn_{75}$ after 300 °C annealing, which leads to the increase of exchange biased and coercivity fields of the pinned layer. The large H_{EB} and H_{CP} are required for stable switching of MTJ. The enhancement of interlayer coupling energy, good remanence and coercive squareness, and softening of the free layer hysteresis loop are due to the increase of permalloy grains after annealing treatment.

Acknowledgements

This work was partially supported by Ministry of Scientific Research and Information Technology (grant No. PBZ/KBN/044/P03/2001).

References

[1] J. Noguës and Ivan K. Schuller, J. Magn. Magn. Mat. **192**, 203 (1999).
[2] M. Takahashi and M. Tsunoda, J. Phys. D: Appl. Phys. **35**, 2365 (2002).
[3] A. E. Berkowitz and K. Takano, J. Magn. Magn. Mat. **200**, 552 (1999).
[4] M. Pakala, Y. Huai, G. Anderson, and L. Miloslavsky, J. Appl. Phys. **87**, 6653 (2000).
[5] K. Yagami, M. Tsunoda, and M. Takahashi, J. Appl. Phys. **89**, 6609 (2001).
[6] G. Anderson. Y. Huai, and L. Miloslavsky, J. Appl. Phys. **87**, 6989 (2000).
[7] J. van Driel, F. R. de Boer, K.-M. H. Lenssen, and R. Coehoorn, J. Appl. Phys. **88**, 975 (2000).
[8] H. Li, P. P Freitas, Z. Wang, J. B. Sousa, and P. Gogol, J. Chapman, J. Appl. Phys. **89**, 6904 (2001).
[9] K. Hoshino, R. Nakatani, H. Hoshiya, Y. Sugita, and S. Tsunashima, Jpn. J. Appl. Phys. **I35**, 607 (1996).
[10] R. Nakatani, H. Hoshiya, H. Hoshino, and Y. Sugita, J. Magn. Magn. Mat. **173**, 321 (1997).
[11] A. J. Devasahayam, P. J. Sides, and M. H. Kryder, J. Appl. Phys. **83**, 7216 (1998).
[12] M. Tsunoda, K. Nishikawa, S. Ogata, and M. Takahashi, Appl. Phys. Lett. **80**, 3135 (2002).
[13] M. Tsunoda and M. Takahashi, J. Magn. Magn. Mat. **239**, 149 (2002).
[14] S. Foner, Rev. Sci. Instr. **30**, 548 (1959).
[15] A. W. Pacyna, J. Phys. E: Sci. Instrum. **17**, 141 (1984).
[16] J. Wrona, T. Stobiecki, M. Czapkiewicz, and R. Rak, Materials Science **21**, 55 (2003).
[17] J. Wrona, doctor thesis, University of Mining and Metallurgy Krakow, 2002.
[18] J. Wrona, T. Stobiecki, M. Czapkiewicz, R. Rak, T. Œlêzak, J. Korecki, and C. G. Kim, J. Magn. Magn. Mat. to be published, 2004.
[19] J. Wrona, T. Stobiecki, R. Rak, M. Czapkiwicz, F. Stobiecki, L. Uba, J. Korecki, T. Œlêzak, J. Wilgocka-Œlêzak, and M. Roots, Phys. Stat. Sol. (a) **196**(1), 161 (2003).
[20] M. Tsunoda and M. Takahashi, J. Magn. Magn. Mat. **239**, 149 (2002).
[21] J. C. S. Kools, W. Kula, D. Mauri, and T. Lin, J. Appl. Phys. **85**, 4466 (1999).